






Cite this: *J. Mater. Chem. A*, 2018, 6, 22731

# New insight into Na intercalation with Li substitution on alkali site and high performance of O3-type layered cathode material for sodium ion batteries†

Ji Eun Wang, <sup>a</sup> Woo Hyun Han, <sup>b</sup> Kee Joo Chang, <sup>b</sup> Young Hwa Jung <sup>\*c</sup> and Do Kyung Kim <sup>\*a</sup>

Lithium was substituted on the alkali site of an O3-type layered structure as cathode material for sodium-ion batteries (SIBs). Role of Li in Na intercalation and high performance is reported for the first time. The behavior of Na during intercalation is a critical factor that determines electrochemical performance. Although transition-metal oxides with layered structures have been studied extensively for SIBs, the focus has been on substitution at transition metal sites rather than at the alkali site. Here, substitution of Li at the alkali site of  $\text{Na}_x[\text{Fe}_y\text{Mn}_{1-y}]\text{O}_2$  ( $0 \leq x, y \leq 1$ ) layered materials is reported for the first time. The substituted element at the alkali site can directly interfere with the behavior of Na during intercalation. *In situ* XRD, synchrotron powder XRD, neutron powder diffraction, *ex situ* XANES, and DFT calculation revealed that Li at alkali sites stabilized the layered structure during the electrochemical reaction and assisted Na intercalation by lowering the energy barrier for Na-hopping. Contrary to common understanding, Li substituted material showed an improved cyclic and rate performance in spite of the smaller interlayer spacing of the O3-type layered structure. The result provides new insight into the role of a substituted element at the alkali site and shows that the Li at the alkali site is a key factor for achieving high performance of a layered cathode material.

Received 26th June 2018  
Accepted 19th October 2018

DOI: 10.1039/c8ta06159a

rsc.li/materials-a

## Introduction

The demand for large-scale applications of lithium-ion batteries (LIBs) is growing rapidly. The price of lithium resources has been increasing quickly because of the expansion of the LIB market and almost 40% of lithium resources are now consumed by battery applications in the United States.<sup>1</sup> Sodium-ion batteries (SIBs) have received much attention for large-scale applications because sodium (Na) is abundant in the Earth's crust and cheap, and is therefore suitable as an alternative candidate to LIBs for large-scale applications.<sup>2</sup>

Transition metal (TM) oxides with layered structures have been studied extensively as cathode materials for SIBs.<sup>3–5</sup> The layered structures of TM oxides that have been studied as electrode materials usually fall into one of two categories, *i.e.*,

P2-type or O3-type layered structures, based on the notation reported by Delmas *et al.*<sup>6</sup> In the layered structure, edge-sharing  $\text{MeO}_6$  (Me = transition metals) octahedra form the TM layer of  $(\text{MeO}_2)_n$ , and the alkali metal located between the TM layers forms an alkali-metal layer. Sodium (Na) ions undergo repeated insertion/deinsertion into a host layered material during the charge/discharge process as an electrode material for SIBs. The behaviour of Na during insertion/deinsertion would depend on various factors such as composition, layer structure, and neighbouring environment.

Commonly used approaches for improving the electrochemical properties of TM oxides as electrode materials for SIBs include varying the composition and substituting foreign elements, such as electrochemically active transition metals (Fe, Mn, Ti, Ni, Co, *etc.*) and/or electrochemically inactive elements (Al, Zn, Li, Mg, Ca, *etc.*).<sup>3,5,7–16</sup> Fe- and Mn-based layered materials, in particular, have received much attention because they consist of earth-abundant elements and have good reversible capacities.<sup>17–20</sup> Previous literatures mostly focused on the substitution at transition metal site (TM site) rather than at alkali site because TM and the substituted elements often have similar ionic radii. Substitution at the TM site could affect the redox behavior and structure of the layered material, leading to improved electrochemical properties. Substitution at the alkali

<sup>a</sup>Department of Materials Science and Engineering, Korea Advanced Institute of Science and Technology (KAIST), 291 Daehak-ro, Yuseong-gu, Daejeon, 34141, Republic of Korea. E-mail: dkkim@kaist.ac.kr

<sup>b</sup>Department of Physics, Korea Advanced Institute of Science and Technology (KAIST), 291 Daehak-ro, Yuseong-gu, Daejeon, 34141, Republic of Korea

<sup>c</sup>Pohang Accelerator Laboratory (PAL), 80 Jigokro-127-beongil, Nam-gu, Pohang, Gyeongbuk, 37673, Republic of Korea. E-mail: yhjung@postech.ac.kr

† Electronic supplementary information (ESI) available. See DOI: 10.1039/c8ta06159a

sites could directly affect the intercalation/deintercalation of alkali metals by changing the interlayer distance and interfering with diffusion paths.<sup>21</sup> However, there are relatively few reports of substitution at the alkali sites in layered structures.

Previous reports of alkali site substitution are limited to elements that have a similar or larger ionic radius. In LIB systems, substitution at alkali sites involved larger cations such as  $\text{Ca}^{2+}$  (1.00 Å) or  $\text{Na}^+$  (1.02 Å) to enlarge the interlayer spacing and widen the intercalation path for  $\text{Li}^+$  (0.76 Å). Huang *et al.*<sup>22</sup> investigated the effects of substitution of a large element (Na) for a smaller element (Li) in the layered structure of LIBs. The results indicate that the introduction of a larger element increased the interlayer spacing, leading to good capacity retention and a superior rate capability. Han *et al.*<sup>15</sup> substituted Ca for Na at alkali sites in an SIB system. Because the ionic radius of  $\text{Ca}^{2+}$  is similar to that of Na, it was successfully substituted at alkali sites. Substitution by Ca improved the average diffusion coefficient.

In this paper, we propose a novel approach to substituting smaller cations ( $\text{Li}^+$ ) at alkali sites of  $\text{Na}_x[\text{Fe}_y\text{Mn}_{1-y}]\text{O}_2$  ( $0 \leq x, y \leq 1$ ) and reveal Li-assisted Na intercalation behaviour, *i.e.* pseudo-tetrahedral Na-hopping. Substitution of Li in layered materials for SIBs was often focused on TM sites because the ionic radius of Li is closer to that of the TM than to that of Na.<sup>23–27</sup> Here, the Li substitution sites were controlled by adjusting the composition of Fe and Mn, using their difference in stability under different oxidation states. The substitution site of Li was confirmed by synchrotron powder X-ray diffraction (SPXRD), neutron powder diffraction (NPD), X-ray absorption near edge structure (XANES) analysis, and inductively coupled plasma-optical emission spectroscopy (ICP-OES) analysis. *In situ* synchrotron X-ray diffraction (XRD) analysis revealed that substituted Li stabilized the layered structure and suppressed phase transformation. Furthermore, density functional theory (DFT) calculations revealed that Li at the alkali site lowers the energy barrier of adjacent Na-hopping by enabling pseudo-tetrahedral Na-hopping. The electrochemical performance was improved despite the smaller interlayer spacing, which may seem contradicting with a common understanding that a larger interlayer spacing is beneficial for the intercalation/deintercalation of Na and for electrochemical performance. The result indicates that substitution of Li at the alkali site of the layered structure stabilizes the structure and enables pseudo-tetrahedral Na-hopping, playing a critical role in overcoming the smaller interlayer spacing and improving electrochemical performance.

## Results and discussion

There are two possible substitution sites for Li in the layered structure of TM oxide: *i.e.*, TM sites (Fig. 1a) and alkali sites (Fig. 1b). Assuming the same crystal structure and no oxygen deficiency, the oxidation states of the TM depend on the substituted element and its position in order to achieve charge neutrality. Because the oxidation state of Li (+1) is lower than that of TM (often between +2 and +4), Li substitution at TM sites requires higher oxidation states of the TM (Fig. 1a). The result is

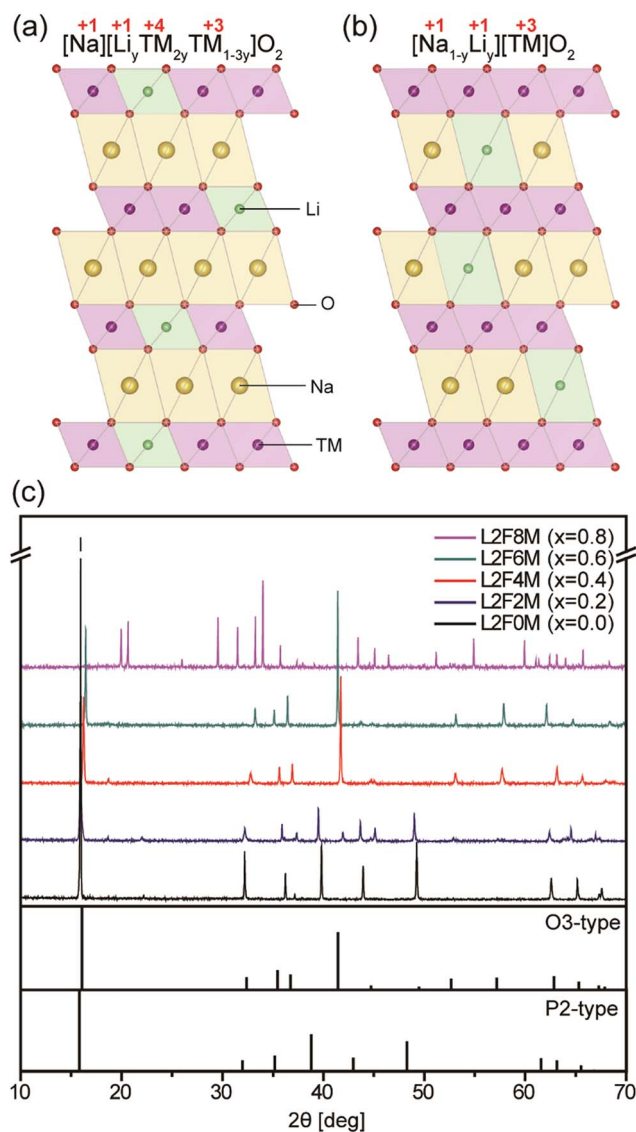


Fig. 1 Schematic figures of two possible substitution sites of Li in an O3-type layered structure – (a) substitution of Li on the transition metal site and (b) substitution of Li on the alkali site. Transition metal atoms are shown in violet, O atoms in red, Na atoms in yellow, and substituted Li atoms in green. (c) XRD patterns of Li-substituted  $\text{Na}_{0.67}\text{Li}_{0.2}\text{Fe}_x\text{Mn}_{0.8-x}\text{O}_2$ . A difference in crystal structure and lattice parameter can be observed depending on the ratio between Fe and Mn.

an increase in the average oxidation state of the TM. If Li is substituted at alkali sites, the TM does not need to have a higher oxidation state because Li has the same oxidation state as Na (Fig. 1b).

This also indicates that the Li substitution site would depend on the TM. The ionic radius of  $\text{Li}^+$  (0.76 Å) is closer to those of TM ( $\text{Fe}^{3+}$ ,  $\text{Mn}^{3+} = 0.645$  Å) than to that of  $\text{Na}^+$  (1.02 Å). Therefore, it was often assumed in previous studies that Li would be substituted at TM sites.<sup>25,26</sup> This assumption would be reasonable if the higher oxidation state of the TM were stable. However, if the higher oxidation state of the TM were not stable, then Li substitution at alkali sites would be preferred.

Therefore, it would be possible to induce the preferential substitution of Li at specific sites by controlling the TM composition.

To clarify the effect of the TM composition on the Li substitution sites, five different samples with a composition of  $\text{Na}_{0.67}\text{Li}_{0.2}\text{Fe}_x\text{Mn}_{0.8-x}\text{O}_2$  ( $0.0 \leq x \leq 0.8$ ) were prepared and are denoted L2F0M ( $x = 0.0$ ), L2F2M ( $x = 0.2$ ), L2F4M ( $x = 0.4$ ), L2F6M ( $x = 0.6$ ), and L2F8M ( $x = 0.8$ ). Varying the Fe/Mn composition would affect the overall stability of the TM in a high oxidation state because  $\text{Fe}^{4+}$  is less stable than  $\text{Mn}^{4+}$ . If a high oxidation state of the TM element is stable enough, Li would be substituted at the TM site. The result is an Na-deficient TM oxide [ $\text{Na}_{0.67}\text{Li}_{0.2}\text{Fe}_x\text{Mn}_{0.8-x}\text{O}_2$ ]. In this case, the material has the P2-type layered structure because of the deficiency of alkali sites.<sup>6,7</sup> The XRD pattern of L2F0M shows a pure P2-type layered structure. This indicates that Li was substituted at the TM sites of L2F0M and the resulting average oxidation state of TM is +3.91.

If the high oxidation state of the TM is not stable enough, then Li substitution at alkali sites would be preferred to substitution at the TM site. This gives a TM oxide with a high occupancy of alkali sites: *i.e.*, [ $\text{Na}_{0.67}\text{Li}_{0.2}$ ][ $\text{Fe}_x\text{Mn}_{0.8-x}\text{O}_{1.6}$ ]. Previous studies have shown that the O3-type layered structure is stable when Na occupancy is high because octahedral sites for Na ions are more closely packed than the relatively spacious prismatic sites.<sup>3,6</sup> Therefore, it is possible to infer that when Li is substituted at alkali sites, an O3-type layered structure would be preferred because both Na and Li occupy alkali sites. Both L2F4M and L2F6M are O3-type, indicating that Li was substituted at the alkali sites because of the higher Fe/Mn ratio and the instability of the  $\text{Fe}^{4+}$  state. The resulting compositions of L2F4M and L2F6M are [ $\text{Na}_{0.67}\text{Li}_{0.2}$ ][ $\text{Fe}_{0.4}\text{Mn}_{0.4}$ ] $\text{O}_{1.6}$  and [ $\text{Na}_{0.67}\text{Li}_{0.2}$ ][ $\text{Fe}_{0.6}\text{Mn}_{0.2}$ ] $\text{O}_{1.6}$ , respectively.

L2F2M has both P2-type and O3-type layered structures. This can be understood as an intermediate state between a low Fe/Mn ratio (L2F0M) and high Fe/Mn ratio (L2F4M and L2F6M). For L2F8M, a layered structure was not formed. The O3-type  $\text{NaFeO}_2$  phase can be synthesized at a low temperature (650 °C);<sup>8</sup> therefore the synthesis temperature (900 °C) in this study is not appropriate for the synthesis of a layered phase.

Additionally, L0F4M ( $\text{NaFe}_{0.5}\text{Mn}_{0.5}\text{O}_2$ ), L1F4M ( $\text{Na}_{0.9}\text{Li}_{0.1}\text{Fe}_{0.5}\text{Mn}_{0.5}\text{O}_2$ ) and L4F4M ( $\text{Na}_{0.6}\text{Li}_{0.4}\text{Fe}_{0.5}\text{Mn}_{0.5}\text{O}_2$ ) were synthesized and Rietveld refinement of SPXRD patterns were conducted to confirm that Li is substituted at alkali sites when  $\text{Fe}/\text{Mn} \geq 1$  (Fig. 2a and Table S1†). The major phase of all samples matched the O3-type layered structure, indicating that the samples have a high occupancy of alkali sites because Li was substituted at the alkali sites. The results support the idea that the Li substitution sites can be controlled by adjusting the TM composition.

Detailed SPXRD pattern and Rietveld refinement results of L2F4M are shown in Fig. S1 and Table S1.† Some previous reports have reported that the substitution of Li resulted in a composite P2/O3-type layered structure.<sup>28,29</sup> The Rietveld refinement result showed that L2F4M consisted of an O3-type (trigonal space group  $R\bar{3}m$ ) layered structure and  $\text{Li}_2\text{MnO}_3$  phase. Diffraction peaks of L2F4M did not match the P2-type layered structure (hexagonal space group  $P6_3/mmc$ ).

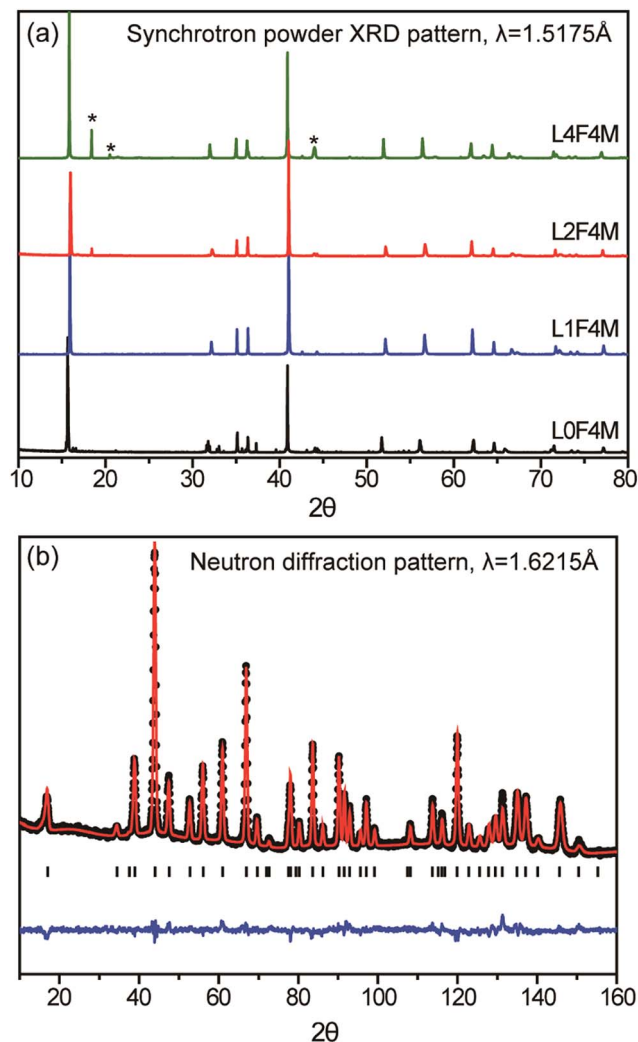


Fig. 2 (a) SPXRD patterns of L0F4M, L1F4M, L2F4M, and L4F4M. The amount of  $\text{Li}_2\text{MnO}_3$  impurity phase, represented with an asterisk (\*), increases with an increasing amount of substituted Li. (b) Rietveld refinement result of the NPD pattern of L1F4M. The refinement results of diffraction patterns shown in (a) and (b) are summarized in Table S1.† The results support the idea that Li was substituted at the alkali site of the O3-type layered structure.

It was also notable that the amount of  $\text{Li}_2\text{MnO}_3$  impurity increased with an increase in Li content. L1F4M did not have any trace of  $\text{Li}_2\text{MnO}_3$  impurity, whereas L2F4M and L4F4M contained 8.4% and 26.2%, respectively. Since the ICP-OES results (Table S2†) corresponded to the designed composition of each sample, the increasing amount of impurity phase indicates that there is a limit to the solubility of Li in TM oxides. The phase ratio result from Rietveld refinement and ICP-OES results for L2F4M were used to calculate the approximate composition of the L2F4M sample (shown below). The solubility limit of Li in the alkali site was calculated to be approximately 15%.



The Rietveld refinement results also showed that the lattice parameters changed depending on the amount of substituted Li

(Table S1†). Compared with L0F4M, the lattice parameter  $c$  decreased and  $a$  increased with an increase in the amount of Li substitution for L1F4M and L2F4M. Assuming Li was substituted at the alkali site, the average oxidation states of the TM in L0F4M, L1F4M, and L2F4M are +3.17, +3.14, and +2.98, respectively. It can be inferred that the increasing lattice parameter  $a$  was the result of a lower oxidation state. The decrease in  $c$  can be related to the smaller ionic radius of the Li than that of Na. The decrease in  $c$  and increase in  $a$  could not be explained when Li was assumed to be substituted at the TM site. The changes in lattice parameters also confirm that the Li would be substituted at the alkali site.

In L4F4M, the lattice parameter  $c$  increased. This suggests that the actual amount of substituted Li in L4F4M may be much lower than the intended amount because the majority of Li was incorporated into the  $\text{Li}_2\text{MnO}_3$  impurity phase instead of being substituted.

Rietveld refinement of the NPD pattern of L1F4M was performed (Fig. 2b and Table S1†). Two possible Li coordinations, Li at alkali sites ( $\text{Li}_{\text{Na}}$ ) with (0, 0, 1/2) coordination and Li at transition-metal sites ( $\text{Li}_{\text{TM}}$ ) with (0, 0, 0) coordination, were considered in the Rietveld refinement of the NPD results, and the Li occupancy at each site was refined. The refinement results show that the majority of substituted Li occupies alkali sites.

Substitution of Li at alkali sites was further confirmed by *ex situ* XANES analysis at the Fe-K and Mn-K absorption edges (Fig. 3 and S2†). *Ex situ* electrodes of L0F4M and L2F4M in the open-circuit voltage (OCV) state, at 4.5 V after the first charge process, at 1.5 V after the first discharge process, and at 4.5 V after the second charge process were prepared and analysed. *Ex situ* electrodes of L0F4M are compared in Fig. 3a and b. The absorption spectra of the Fe-K edge in the OCV state was closer to that at 1.5 V, indicating lower oxidation state of Fe. The Mn-K edge of L0F4M in the OCV state was positioned between the discharged state and the charged state. This could be due to Na deficiency in L0F4M, as shown in Table S2.† The reversible shift in the Fe-K and Mn-K absorption spectra of L0F4M indicates a reversible redox reaction of both Fe and Mn, which is consistent with a previous report.<sup>19</sup>

Fig. 3c and d show the absorption spectra of L2F4M at the Mn-K and Fe-K edges. They shifted reversibly between the charged and discharged states. The reversible shift of the absorption spectra indicates that both Mn and Fe participated reversibly in the electrochemical redox reaction in L2F4M. The oxidation states of Mn and Fe in the OCV electrode of L2F4M were similar to the oxidation state at 1.5 V. It can be inferred that the as-synthesized L2F4M consisted of Mn and Fe with relatively low oxidation states, which supports that Li was substituted at alkali sites in L2F4M.

The electrochemical performance of Li-substituted L1F4M and L2F4M were compared with that of L0F4M (Fig. 4). L2F4M showed a superior cycle life, with 80.7% capacity retention after 100 cycles, while L0F4M showed 36% capacity retention after 100 cycles. Even after 200 cycles, L2F4M showed 72% capacity retention (close to  $180 \text{ mA h g}^{-1}$ ). L2F4M also showed an improved rate capability, with a capacity of  $59 \text{ mA h g}^{-1}$  at

a current density of  $200 \text{ mA h g}^{-1}$ . L1F4M also showed better capacity retention than L0F4M, showing that Li substitution on the alkali site led to improved capacity retention of the O3-type layered structure.

L2F4M showed a sloppy discharge profile without any evident voltage plateau, which indicates a smooth solid-solution reaction throughout the discharge. A short plateau was observed in the initial stage of the charge profile, which implies a phase transition in this voltage range. Further discussion regarding the phase transition of L2F4M is addressed in a later section with *in situ* XRD results. The voltage plateau of L1F4M (Fig. S3†) showed a similar tendency to that of L2F4M. The voltage profile of L0F4M showed a fast increase in IR drop while L2F4M showed a stable profile up to 100 cycles.

It is notable that L2F4M showed a better rate capability and cycle life although its interlayer distance of  $5.4642 \text{ \AA}$  is smaller than that of L0F4M's  $5.5640 \text{ \AA}$  (Table S1†). Previous studies have shown that larger interlayer distances improved Na diffusion and the electrochemical performance of layered TM oxides because the enlarged interlayer distance provided a larger diffusion path for Na intercalation.<sup>19,22,30</sup> However, L2F4M gave better performance, which shows that substitution of Li at alkali sites greatly improved the electrochemical properties of layered materials, and the improvement was enough to overcome the disadvantages of smaller interlayer distances. This will be discussed in the following section using DFT calculation.

*Ex situ* ICP-OES analysis, *in situ* synchrotron XRD analysis, and DFT calculations of energy barriers were conducted to clarify the role of Li at alkali sites. *Ex situ* ICP-OES (Table S3†) showed that the Li contents after the first charge and first discharge were similar. Compared with the changes in Na content, the Li content of the *ex situ* electrodes did not change much. The result indicates that Li did not actively participate in intercalation/deintercalation processes and would not contribute to the capacity. Instead, it seems to stay within the active material without participating in intercalation during cycling.

A Li half-cell with L2F4M was assembled to investigate Li migration in this structure. The voltage profile for the Li half-cell during the first charge was similar to that of an Na half-cell (Fig. S4†), indicating that the initial desodiation behaviour was similar. During first discharge, almost 0.6 Na was re-inserted into the structure after desodiation of 0.66 Na in the Na half-cell. In contrast, only 0.2 Li was re-inserted into the L2F4M structure in the Li half-cell. This suggests that Li intercalation in L2F4M is less preferred than Na intercalation and that within the Na half-cell, Na is much more likely to participate in electrochemical reactions than Li.

*In situ* synchrotron XRD analysis showed that inactive Li at alkali sites stabilized the layered structure during charge/discharge processes. In Fig. 5a, the overall peak shift during the first charge clearly indicates a phase transformation from O3 to P3-type layered structures. Once the phase transformation was completed after the first charge, the P3-type phase was stable throughout the discharge processes, undergoing stable solid-solution reactions across a wide voltage range. The lattice parameter  $c$  of the P3-type layered structure decreased smoothly



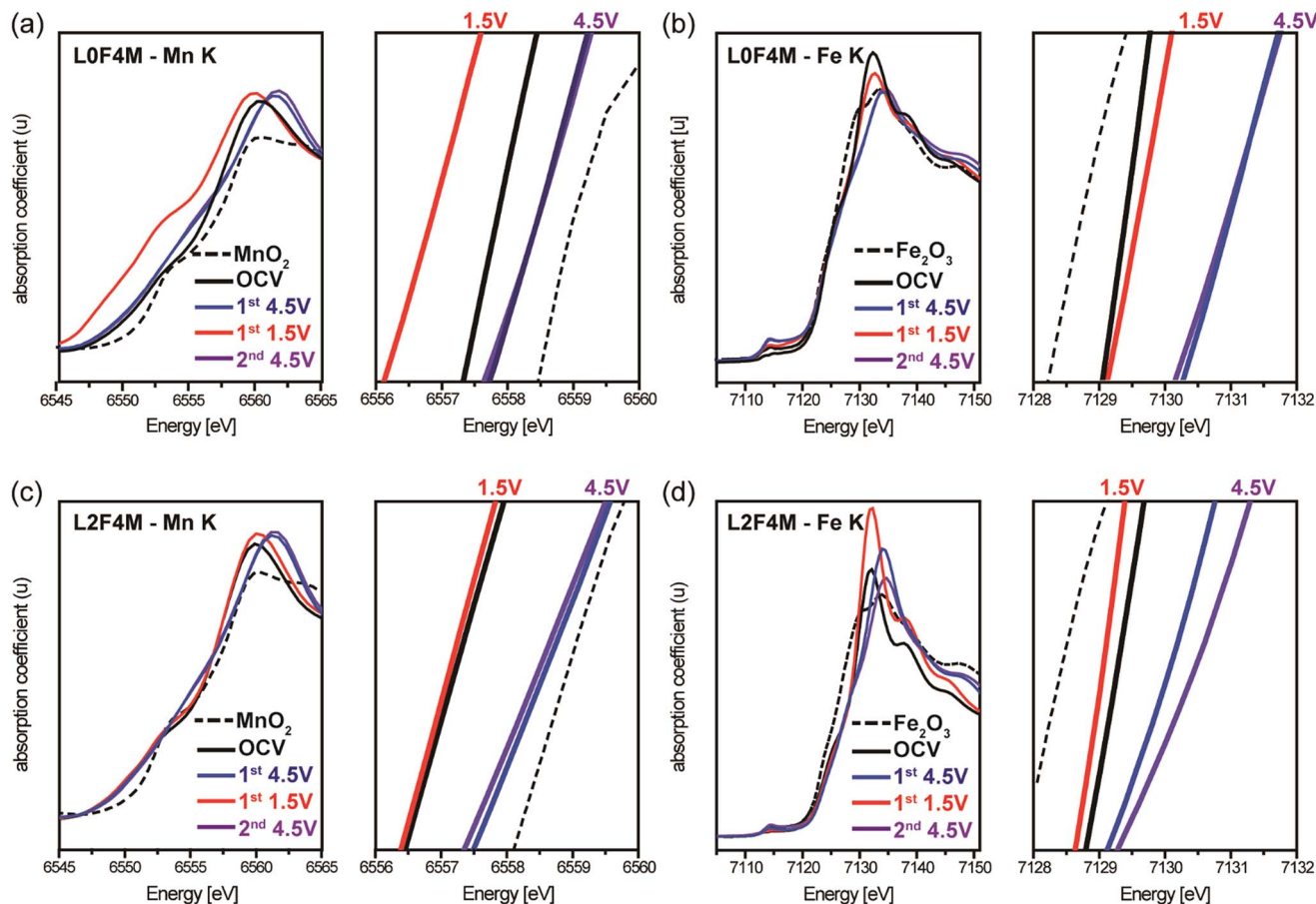


**Fig. 3** *Ex situ* XANES spectra at (a) the Mn-K absorption edge of L0F4M, (b) the Fe-K absorption edge of L0F4M, (c) the Mn-K absorption edge of L2F4M, and (d) the Fe-K absorption edge of L2F4M with  $\text{MnO}_2$  and  $\text{Fe}_2\text{O}_3$  spectra as reference oxides. Electrodes in the open circuit voltage (OCV) state are represented in black. *Ex situ* electrodes at 4.5 V after the first charge process are represented in blue and *ex situ* electrodes at 4.5 V after the second charge process in violet. *Ex situ* electrodes at 1.5 V after the first discharge process of the first cycle are represented in red. The reference oxide spectra are represented by black, dashed lines. The absorption spectra of *ex situ* electrodes showed a reversible redox reaction of Fe and Mn in both samples.

and changed by only  $-0.37\%$  during the first discharge (Fig. 5b). The solid-solution reaction throughout the discharge process corresponds to the sloppy discharge voltage profile of L2F4M.

The O3-type layered structure reappeared at the final stage of the second discharge. The appearance of an O3-type layered structure can be identified by the intensity of the (104) peak around  $22^\circ$  in Fig. 5a. A small fraction was transformed from a P3-type to an O3-type layered structure in a low voltage region (below 2.0 V). The diffraction peaks of the O3-type layered structure were clearer in the second charge process. The smaller peak intensities of the O3-type structure during the first discharge than during the second charge may have been caused by the large current density and fast phase transformation under the *in situ* experimental conditions. Based on previous studies, it is reasonable to expect the formation of the O3-type structure in the low voltage region (below 2.0 V).<sup>20</sup> The O3-type layered structure was transformed to a P3-type layered structure again during the second charge. Although the O3-type layered structure appeared, the P3-type layered structure was found as a major phase even in low-voltage regions.

A previous study of O3-type  $\text{Na}[\text{Fe}_{0.5}\text{Mn}_{0.5}]\text{O}_2$  reported an O3-P3-OP2 type phase transformation,<sup>20</sup> in which the material maintained P3 type only between 2 and 4 V. However, when Li was substituted at the alkali sites, the P3-type layered structure remained as major phase during the first discharge process and subsequent charge/discharge process. It can be inferred that the substitution of Li at alkali sites resulted in a stable P3-type layered structure throughout the charge/discharge process and the absence of multiple phase transitions resulted in an improved electrochemical performance.

The short plateau at around 2.3 V in the charge voltage profile of L2F4M corresponds to the two-phase reaction shown in the *in situ* XRD results. In the two-phase region in the second charge process, the lattice parameter  $c$  of the O3-type structure changed from 16.456 Å to 16.55 Å, whereas the  $c$  of the P3-type structure was almost constant, with an average value of 16.809 Å. When the O3-type layered structure could no longer be observed, the lattice parameter  $c$  of the P3-type layered structure increased from 16.809 Å to 16.850 Å, showing only a 0.24% increase.

To understand the behaviour of Li at alkali sites and its effect on the energy barrier of Na intercalation, we performed DFT

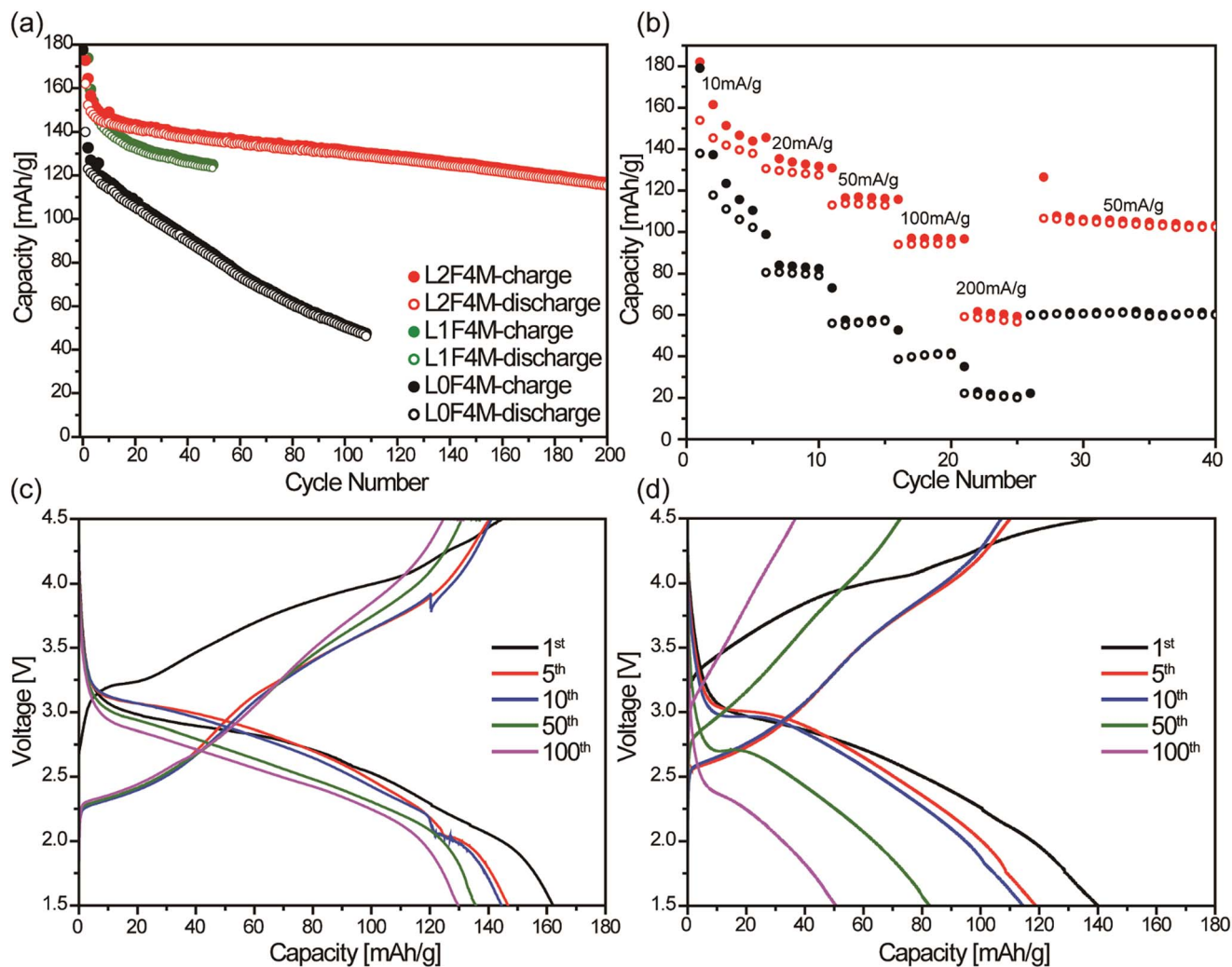


Fig. 4 (a) Electrochemical charge/discharge test under constant current, (b) rate capability test of L0F4M and L2F4M, and corresponding voltage profile of (c) L2F4M and (d) L0F4M during a charge/discharge test.

calculations. The calculation was focused on the O3-type layered structure because intercalation of Na through the octahedral sites of the O3-type layered structure has been reported to be more difficult than that of prismatic sites.<sup>19</sup> The O3-type layered structure was found at an initial stage of the first charge and in the low voltage regions of subsequent cycles. Therefore, the energy barrier of Na intercalation in the O3-type layered structure would be the highest barrier throughout the charge/discharge process and would significantly affect the overall energy barrier of Na intercalation.

The Na diffusion path that connects two adjacent octahedral sites in the O3-type layered structure can be one of two types, namely a tetrahedral hop or a dumbbell hop, depending on the local environment of the Na vacancy. The tetrahedral hop is preferred when there are two adjacent Na vacancies, and has a lower hopping energy barrier than a dumbbell hop under the same lattice parameter conditions.<sup>19</sup> In this case, Na passes through an adjacent tetrahedral site before reaching an adjacent Na vacancy (octahedral site). The dumbbell hop occurs when there is only one adjacent Na vacancy. It has a higher

hopping energy barrier because Na has to pass through two oxygen atoms in dumbbell positions. In the DFT calculations, we assumed a dumbbell hop with one adjacent Na vacancy and one adjacent Li in the O3-type layered structure in order to clarify the effect of Li on the Na-hopping. This condition was chosen because a larger energy barrier for a dumbbell hop would represent the overall Na diffusion barrier.

In the calculation, one Na vacancy was assumed in a  $3 \times 3 \times 1$  super cell structure and an Li substitution site was assumed to be adjacent to the Na vacancy. The calculation focused on one sodium layer, which contained an Na vacancy and two adjacent oxygen layers. We calculated the energy barriers with lattice parameters of L0F4M or L2F4M, without or with Li, respectively. The energy barrier tends to increase as the interlayer distance decreases when the atomic compositions are identical (Fig. S5<sup>†</sup>). Calculations also indicate that Li substitution decreased the energy barrier for Na-hopping, regardless of the interlayer distance. Interestingly, the energy barrier of L2F4M (lattice parameter of L2F4M, with Li) was lower than that of L0F4M (lattice parameter of L0F4M, without Li) although it had

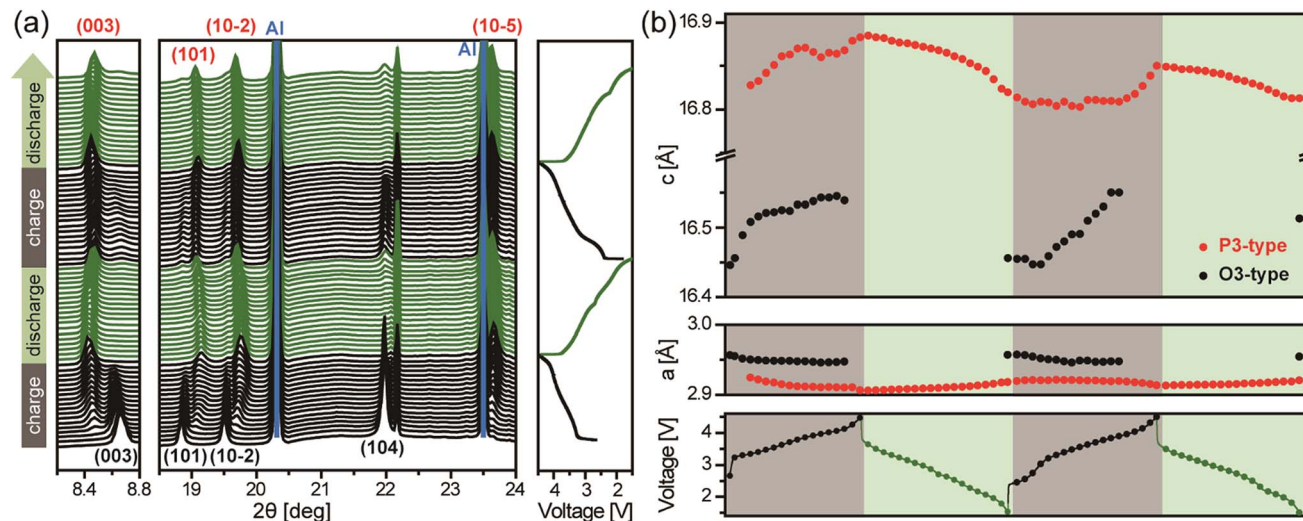


Fig. 5 (a) *In situ* synchrotron XRD analysis patterns and (b) refined lattice parameter change during the first and second cycles. (*hkl*) are shown in black for an O3-type structure and in red for a P3-type structure. Aluminium peaks are noted in blue. The peak shift shows that the O3-type structure is transformed into a P3-type structure during the first charge. Then, a P3-type layered structure can be found as a major phase throughout the charge and discharge process, which indicates that the P3-type structure has been stabilized by substituted Li.

a smaller interlayer distance (Fig. 6a). The smaller interlayer spacing of L2F4M would have resulted in a larger energy barrier were it not for the beneficial effect of Li substitution (indicated by energy barrier of lattice parameter of L2F4M/without Li and lattice parameter of L2F4M/with Li). It is apparent that the substitution of Li at alkali-sites assisted Na-hopping by lowering the energy barrier enough to overcome the disadvantage that was caused by the smaller interlayer distance. This result agrees well with the experimental observation of enhanced Na diffusion in the presence of Li.

Fig. 6b–d show the initial, intermediate, and final configurations of L2F4M during the Na migration. For each configuration, the atomic structure was viewed from the (001) and (011) directions. In the initial stage, one Li atom (green) was positioned adjacent to the Na vacancy to which the Na atom (orange) will hop. In the final stage, the hopping Na atom occupied the vacant site. It is interesting to note that, in the intermediate configuration, Li relaxed away from the Na-hopping path and the  $\text{LiO}_6$  octahedron was slightly distorted (Fig. 6e and f). Because the atomic size of Li is smaller than that of Na, Li had more freedom to move within the octahedron and thus widened the Na-hopping path. Because of the widened path, Na no longer passed through the oxygen dumbbell. The traces of Li (green) and Na (orange) throughout hopping process are marked as translucent circles in Fig. 6c and d. As Li was relaxed away from Na, Na passed closer to the tetrahedral site, although there was only one adjacent Na vacancy. Compared to the initial position of Li, Li was relaxed away from Na by 0.623 Å in the intermediate state. The position of Na in the intermediate state with Li substitution was closer to the tetrahedral site by 0.414 Å compared to the position of Na during dumbbell hopping (Fig. 6g). Such behaviour of Na-hopping can be understood as pseudo-tetrahedral hopping, where the Na-hopping path was similar to tetrahedral hopping although there was only one adjacent Na vacancy. The octahedral distortion and the

resulting pseudo-tetrahedral Na-hopping could only occur with Li substitution. The lower energy barriers and overall improvements in the electrochemical performances of Li-substituted structures can therefore be attributed to both stable P3-type layered structure and pseudo-tetrahedral hopping in Na diffusion, assisted by Li at alkali sites.

Similarly, an energy barrier calculation was made with a P3-type layered structure. The calculation was conducted under the assumption that the Li is at a prismatic site in the alkali layer and that 2/3 of Na sites are filled. The same calculation method was used with the superstructure cell. The energy barrier per Na atom in the P3-type layered structure showed a much lower energy barrier (approximately 30 meV) than that of the O3-type, which corresponds with previous literature.<sup>19</sup> Also, the effect of Li on the energy barrier was negligible, which would be due to Na vacancies and the longer distance between alkali elements. The calculation result also confirmed that the energy barrier in the O3-type layered structure is a major barrier that determines overall Na diffusion during the charge/discharge process and that the role of Li in the O3-type layered structure is a critical factor. The low energy barrier in the P3-type layered structure also indicates that the stable P3-type structure throughout the charge/discharge process, as shown by *in situ* XRD, led to improved electrochemical performance.

## Experimental

### Material synthesis

Active materials were synthesized by a simple solid-state method from  $\text{Na}_2\text{CO}_3$  (ACS reagent, anhydrous, Sigma-Aldrich, Darmstadt, Germany),  $\text{Li}_2\text{CO}_3$  (99+%, Junsei, Tokyo, Japan),  $\text{Mn}_3\text{O}_4$  (97%, Sigma-Aldrich, Darmstadt, Germany), and  $\text{Fe}_3\text{O}_4$  ( $\geq 95\%$ , Samchun Chemical, Pyeongtaek-si, Republic of Korea) powders as precursors. Stoichiometric amounts of the precursors were thoroughly mixed in a mortar until a homogeneous mixture was



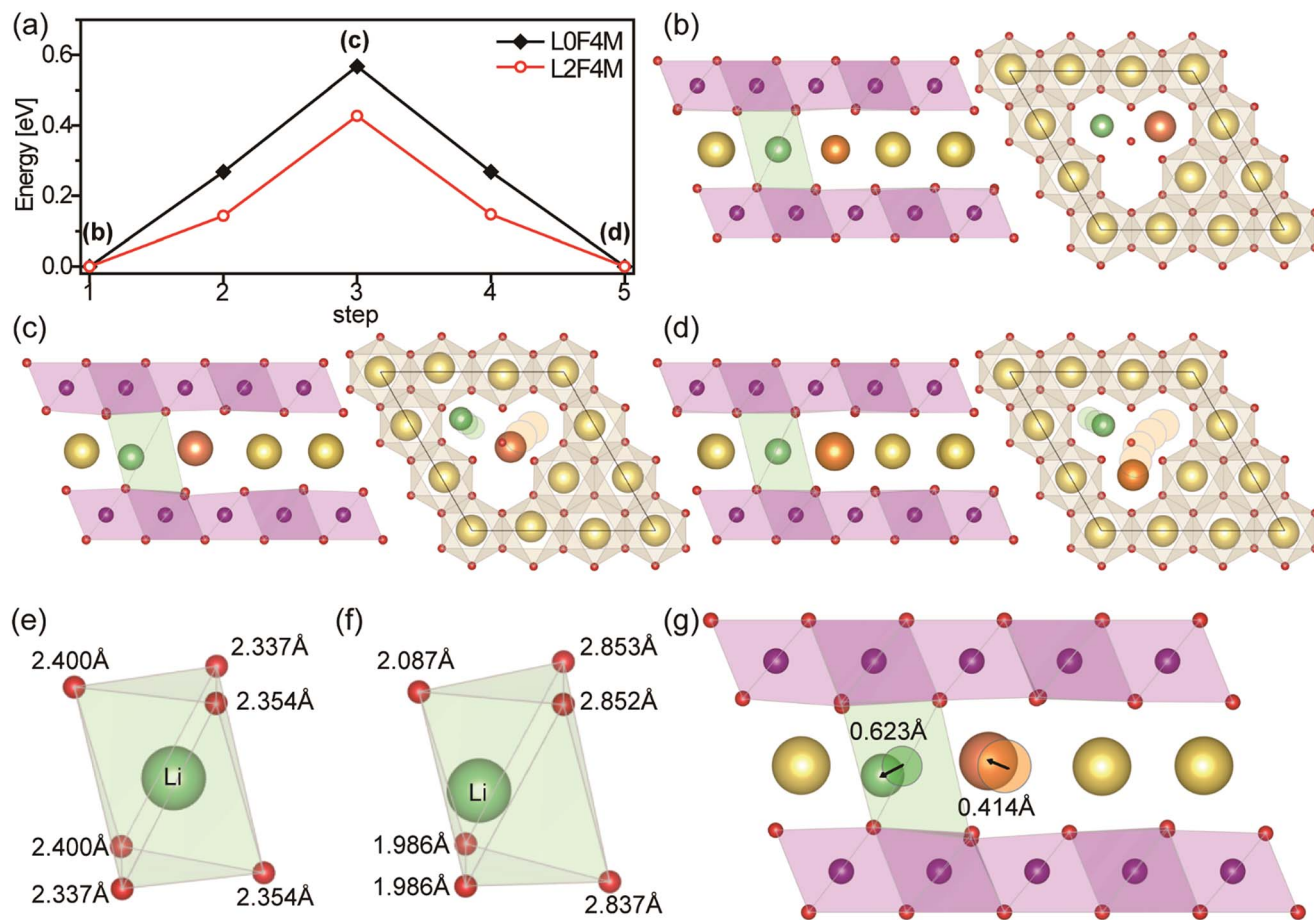


Fig. 6 (a) Calculated energy barriers for Na dumbbell hop for L0F4M and L2F4M. Schematic illustration of L2F4M at (b) initial, (c) intermediate, and (d) final configuration of Na-hopping in the presence of an Na vacancy and substituted Li. Detailed schematic of LiO<sub>6</sub> octahedral (e) in initial and (f) in intermediate configurations. The numbers indicate the distance between Li and each O atom. (g) Displacement of Li and Na during pseudo-tetrahedral hopping compared with dumbbell hopping. The position of the adjacent Li is displaced away from Na by 0.623 Å. The position of the hopping Na is displaced by 0.414 Å when Na undergoes pseudo-tetrahedral hopping rather than dumbbell hopping. Transition metal atoms are shown in violet, O atoms in red, Na atoms in yellow, substituted Li atoms in green, and the moving Na atoms in orange.

formed. The mixed precursors were then formed into pellets with diameters of 14 mm. The pellets were heat-treated in a box furnace at 900 °C for 12 h in air. After heat-treatment, the pellets were ground into fine powders and kept in a glove box with an inert Ar atmosphere. Five materials with different Fe/Mn ratios were synthesized. The Na<sub>0.67</sub>Li<sub>0.2</sub>Fe<sub>x</sub>Mn<sub>0.8-x</sub>O<sub>2</sub> composition varied from  $x = 0.0$  to  $x = 0.8$  and the samples were denoted by L2F0M (Na<sub>0.67</sub>Li<sub>0.2</sub>Mn<sub>0.8</sub>O<sub>2</sub>, no Fe), L2F2M (Na<sub>0.67</sub>Li<sub>0.2</sub>Fe<sub>0.2</sub>Mn<sub>0.6</sub>O<sub>2</sub>, Fe/Mn = 1/3), L2F4M (Na<sub>0.67</sub>Li<sub>0.2</sub>Fe<sub>0.4</sub>Mn<sub>0.4</sub>O<sub>2</sub>, Fe/Mn = 1), L2F6M (Na<sub>0.67</sub>Li<sub>0.2</sub>Fe<sub>0.6</sub>Mn<sub>0.2</sub>O<sub>2</sub>, Fe/Mn = 3), and L2F8M (Na<sub>0.67</sub>Li<sub>0.2</sub>Fe<sub>0.8</sub>O<sub>2</sub>, no Mn). L1F4M (Na<sub>0.9</sub>Li<sub>0.1</sub>Fe<sub>0.5</sub>Mn<sub>0.5</sub>O<sub>2</sub>, Fe/Mn = 1) and L4F4M (Na<sub>0.6</sub>Li<sub>0.4</sub>Fe<sub>0.5</sub>Mn<sub>0.5</sub>O<sub>2</sub>, Fe/Mn = 1) were synthesized by the same method. For comparison with the Li-substituted samples, L0F4M (NaFe<sub>0.5</sub>Mn<sub>0.5</sub>O<sub>2</sub>, Fe/Mn = 1) was also synthesized by a solid-state method at 900 °C for 15 h in air.

### Electrochemical tests

An electrode slurry was prepared by mixing the as-synthesized active material, carbon (super P), and a polyvinylidene

fluoride (PVDF, Sigma-Aldrich, Darmstadt, Germany) binder in mass ratios of 80 : 10 : 10. *N*-Methyl-2-pyrrolidone (Sigma-Aldrich, Darmstadt, Germany) was used as the solvent for the electrode slurry and the mixture was thoroughly mixed in a mortar. The slurry was cast on Al foil and dried in a vacuum oven at 100 °C overnight. The dried electrode was roll-pressed before assembly into a half cell.

CR2032 coin cells were assembled in an Ar-filled glove box, with a glass fiber filter (Whatman, grade GF/D) as a separator, Na metal as the counter electrode, and 1 M NaPF<sub>6</sub> in ethylene carbonate/diethyl carbonate (1/1, v/v) with 2 wt% fluoroethylene carbonate as the electrolyte. Galvanostatic cycling tests were performed with a WBCS3000 cyler (Wonatech). All electrochemical tests were performed at ambient temperature with a potential window of 1.5–4.5 V.

An Li half-cell of the active material was assembled in an Ar-filled glove box with CR2032 coin cell parts, Li metal as the counter electrode, a glass fiber filter as the separator, and 1 M LiPF<sub>6</sub> ethyl carbonate/dimethyl carbonate/ethyl methyl carbonate (3/4/3, PuriEL) as the electrolyte.



## Characterization

XRD patterns of the samples were recorded in the  $2\theta$  range  $10^\circ$  to  $70^\circ$ , using a RIGAKU SmartLab with Cu  $K\alpha_1$  (1.5406 Å) radiation. High-resolution synchrotron powder XRD (SPXRD) data for the samples were obtained using the 9B-HRPD beamline at the Pohang Accelerator Laboratory (PAL) in Pohang, Republic of Korea. SPXRD data were collected at a wavelength of 1.5175 Å in the  $2\theta$  range  $10^\circ$  to  $130.5^\circ$ , with a step size of  $0.01^\circ$ . NPD data for a selected sample (L1F4M) were obtained using the high-resolution powder diffractometer Echidna, operated by the Australian Nuclear Science and Technology Organisation (ANSTO), Australia. The NPD data were collected at a wavelength of 1.6215 Å over the  $2\theta$  range  $4^\circ$  to  $164^\circ$ , with a step size of  $0.05^\circ$ .

Elemental analyses of the as-synthesized powders and *ex situ* electrodes were performed by ICP-OES (Agilent ICP-OES 720). X-ray absorption fine structure (XAFS) analysis of *ex situ* electrode samples prepared from cycled coin cells was performed at the 8C-Nano XAFS beamline of PAL. Absorption energy level calibration was performed with metal foils as references.

*Ex situ* electrode samples were prepared as follows. The cycled coin cells were disassembled in an Ar-filled glove box. The residual salts in the electrodes were washed with ethyl carbonate/diethyl carbonate (1/1, v/v) and the electrodes were dried overnight in an Ar-filled glove box. For elemental analysis, the slurry was scraped from the Al foil after the cycled electrodes were completely dry. For XAFS analysis, the dried electrodes were sealed with Kapton tape to avoid exposure to air and moisture.

*In situ* synchrotron XRD data for the operating batteries were obtained at the 9C-CXS beamline of PAL, at a wavelength of 0.82654 Å. A Pilatus 1M detector was used to obtain two-dimensional patterns, and these were converted to one-dimensional XRD patterns with the Fit2D program. For *in situ* observations of battery cells, modified CR2032 coin cells with holes in the center covered with polyimide films were used. An  $\text{LaB}_6$  standard reference material (NIST SRM 660c, Sigma-Aldrich) was used for calibration. Diffraction data were collected every 4 min while the *in situ* cell was cycled under a current density of  $50 \text{ mA g}^{-1}$  with an SP-200 potentiostat (Biologic) in constant charge mode during the charge/discharge processes. Rietveld refinements of the SPXRD, NPD, and *in situ* SPXRD data were performed using the refinement program GSAS with EXPGUI<sup>31,32</sup> and FullProf Suite.<sup>33,34</sup> For refinement of the SPXRD data, the occupancy values of each element were fixed based on the ICP-OES analysis results for the as-synthesized powder. In refinement of the NPD data, the occupancy values of each element were also refined.

## Density functional theory calculation

Density functional theory (DFT) calculations were performed using the functional form of Perdew, Burke, and Ernzerhof<sup>35</sup> for the exchange-correlation potential and the projector augmented wave potentials,<sup>36</sup> as implemented in the VASP code.<sup>37</sup> The wave functions were expanded in plane waves up to an energy cut-off

of 500 eV and  $k$ -points were generated using the  $10 \times 10 \times 2$  Monkhorst–Pack meshes for Brillouin zone integration. We used the measured lattice parameters from Rietveld refinement and fully optimized the ionic coordinates until the residual forces were less than  $0.01 \text{ eV \AA}^{-1}$ . To calculate the energy barriers for Na migration, we used a climbing image nudged elastic band method<sup>38</sup> for a  $3 \times 3 \times 1$  supercell geometry containing one Na vacancy. Because the Na vacancy migrates within the Na layer containing itself, we focused on the Na layer and its adjacent oxygen layers rather than on other layers far from the Na vacancy.

## Conclusions

Li was substituted at the alkali site of an O3-type layered structure and its role in Na intercalation behaviour and electrochemical performance was studied. The Li substitution sites in TM layered oxide were controlled by varying the composition of Fe and Mn in the TM layer. In L2F4M, Li was successfully substituted at the alkali site of an O3-type layered structure. The substitution site was confirmed by synchrotron and neutron diffraction patterns. Substitution of Li, which is smaller than Na, at alkali sites decreased the interlayer distance but improved the electrochemical performance, which is contrary to common understanding. Detailed analysis showed that substituted Li stabilized the P3-type layered structure during the electrochemical reaction, which, in turn, led to an improved cycle life and rate performance. Furthermore, the calculated energy barrier of Na-hopping in L2F4M was lower than that of L0F4M. The calculation result revealed that Li substitution lowered the energy barrier despite the decreased interlayer distance by allowing pseudo-tetrahedral hopping of Na instead of dumbbell hopping. The pseudo-tetrahedral Na-hopping occurred with assistance from the adjacent Li at the alkali site, and is a unique feature that is reported here for the first time. The result shows that understanding the role of Li at the alkali site is a key factor in the high performance of layered materials.

## Conflicts of interest

There are no conflicts to declare.

## Acknowledgements

This work was supported by National Research Foundation (NRF) of Korea (2016K1A3A1A25003532, 2016R1D1A1B03934138, and 2017R1A2B2010148) funded by Korea government (MSIT and ME). W. H. Han and K. J. Chang were supported by Samsung Science and Technology Foundation under Grant No. SSTFBA1401-08. Authors acknowledge technical support from 9B-HRPD beam line, 8C-nano XAFS beamline, and 9C-CXS beamline of Pohang Accelerator Laboratory (PAL), Pohang, Korea and Echidna of Australian Nuclear Science and Technology Organisation (ANSTO), Australia.

## Notes and references

- 1 U. S. G. Survey, *Mineral commodity summaries 2017*, U.S. Geological Survey, 2017, vol. 1.
- 2 M. D. Slater, D. Kim, E. Lee and C. S. Johnson, *Adv. Funct. Mater.*, 2013, **23**, 947–958.
- 3 M. H. Han, E. Gonzalo, G. Singh and T. Rojo, *Energy Environ. Sci.*, 2015, **8**, 81–102.
- 4 N. Ortiz-Vitoriano, N. E. Drewett, E. Gonzalo and T. Rojo, *Energy Environ. Sci.*, 2017, **10**, 1051–1074.
- 5 K. Kubota, N. Yabuuchi, H. Yoshida, M. Dahbi and S. Komaba, *MRS Bull.*, 2014, **39**, 416–422.
- 6 C. Delmas, C. Fouassier and P. Hagenmuller, *Phys. B+C*, 1980, **99**, 81–85.
- 7 R. J. Clément, P. G. Bruce and C. P. Grey, *J. Electrochem. Soc.*, 2015, **162**, A2589–A2604.
- 8 N. Yabuuchi, H. Yoshida and S. Komaba, *Electrochemistry*, 2012, **80**, 716–719.
- 9 P. F. Wang, H. R. Yao, X. Y. Liu, J. N. Zhang, L. Gu, X. Q. Yu, Y. X. Yin and Y. G. Guo, *Adv. Mater.*, 2017, **29**, 1–7.
- 10 R. J. Clément, J. Billaud, A. Robert Armstrong, G. Singh, T. Rojo, P. G. Bruce and C. P. Grey, *Energy Environ. Sci.*, 2016, **9**, 3240–3251.
- 11 H. Su, S. Jaffer and H. Yu, *Energy Storage Materials*, 2016, **5**, 116–131.
- 12 J.-Y. Hwang, S.-T. Myung and Y.-K. Sun, *Chem. Soc. Rev.*, 2017, **46**, 3529–3614.
- 13 Y. Tsuchiya, K. Takanashi, T. Nishinobo, A. Hokura, M. Yonemura, T. Matsukawa, T. Ishigaki, K. Yamanaka, T. Ohta and N. Yabuuchi, *Chem. Mater.*, 2016, **28**, 7006–7016.
- 14 D. Buchholz, C. Vaalma, L. G. Chagas and S. Passerini, *J. Power Sources*, 2015, **282**, 581–585.
- 15 S. C. Han, H. Lim, J. Jeong, D. Ahn, W. B. Park, K. S. Sohn and M. Pyo, *J. Power Sources*, 2015, **277**, 9–16.
- 16 Y. H. Jung, A. S. Christiansen, R. E. Johnsen, P. Norby and D. K. Kim, *Adv. Funct. Mater.*, 2015, **25**, 3227–3237.
- 17 J. S. Thorne, R. A. Dunlap and M. N. Obrovac, *J. Electrochem. Soc.*, 2013, **160**, A361–A367.
- 18 B. Mortemard de Boisse, D. Carlier, M. Guignard and C. Delmas, *J. Electrochem. Soc.*, 2013, **160**, A569–A574.
- 19 N. A. Katcho, J. Carrasco, D. Saurel, E. Gonzalo, M. Han, F. Aguesse and T. Rojo, *Adv. Energy Mater.*, 2017, **7**, 1–9.
- 20 N. Yabuuchi, M. Kajiyama, J. Iwatate, H. Nishikawa, S. Hitomi, R. Okuyama, R. Usui, Y. Yamada and S. Komaba, *Nat. Mater.*, 2012, **11**, 512–517.
- 21 Y. Mo, S. P. Ong and G. Ceder, *Chem. Mater.*, 2014, **26**, 5208–5214.
- 22 Z. Huang, Z. Wang, Q. Jing, H. Guo, X. Li and Z. Yang, *Electrochim. Acta*, 2016, **192**, 120–126.
- 23 S. Zheng, G. Zhong, M. J. McDonald, Z. Gong, R. Liu, W. Wen, C. Yang and Y. Yang, *J. Mater. Chem. A*, 2016, **4**, 9054–9062.
- 24 S. Zhang, Y. Liu, N. Zhang, K. Zhao, J. Yang and S. He, *J. Power Sources*, 2016, **329**, 1–7.
- 25 M. S. Kwon, S. G. Lim, Y. Park, S. M. Lee, K. Y. Chung, T. J. Shin and K. T. Lee, *ACS Appl. Mater. Interfaces*, 2017, **9**, 14758–14768.
- 26 S. Oh, S. Myung, J. Hwang, B. Scrosati, K. Amine and Y.-K. Sun, *Chem. Mater.*, 2014, **26**, 6165–6171.
- 27 H. Liu, J. Xu, C. Ma and Y. S. Meng, *Chem. Commun.*, 2015, **51**, 4693–4696.
- 28 E. Lee, J. Lu, Y. Ren, X. Luo, X. Zhang, J. Wen, D. Miller, A. DeWahl, S. Hackney, B. Key, D. Kim, M. D. Slater and C. S. Johnson, *Adv. Energy Mater.*, 2014, **4**, 1–8.
- 29 S. Guo, P. Liu, H. Yu, Y. Zhu, M. Chen, M. Ishida and H. Zhou, *Angew. Chem., Int. Ed.*, 2015, **54**, 5894–5899.
- 30 C. P. Laisa, R. N. Ramesha and K. Ramesha, *Electrochim. Acta*, 2017, **256**, 10–18.
- 31 B. Toby, *J. Appl. Crystallogr.*, 2001, **34**, 210–213.
- 32 A. C. Larson and R. B. Von Dreele, *General Structure Analysis System (GSAS)*, 2004, vol. 748.
- 33 J. Rodríguez-Carvajal, *Phys. B*, 1993, **192**, 55–69.
- 34 FullProf Suite, <https://www.ill.eu/sites/fullprof/php/reference.html>.
- 35 J. P. Perdew, K. Burke and M. Ernzerhof, *Phys. Rev. Lett.*, 1996, **77**, 3865–3868.
- 36 P. E. Blöchl, *Phys. Rev. B: Condens. Matter Mater. Phys.*, 1994, **50**, 17953–17979.
- 37 G. Kresse and J. Furthmüller, *Phys. Rev. B*, 1996, **54**, 11169–11186.
- 38 G. Henkelman, B. P. Uberuaga and H. Jónsson, 2000, **113**, 9901–9904.